Computational Imaging and Tomography PDM-DART Paper-4

Priyanjali Goel, *s4406559* and Zixi Yang, *s3449963*

***Abstract*—The Discrete Algebraic Reconstruction Technique (DART)[1] enhances tomographic reconstructions by incorporating prior knowledge of discrete material densities, particularly beneficial for limited data scenarios. However, DART traditionally requires a priori knowledge of these densities and segmentation thresholds. The Projection Distance Minimization DART (PDM-DART) algorithm automates this by adaptively estimating these parameters. This paper details an implementation of the PDM-DART framework, featuring specific extensions: initialization of grey levels and thresholds using Gaussian Mixture Models (GMM) applied to an initial SIRT reconstruction, intended to provide a more data-driven starting point, and a median filtering step for post-processing designed to reduce residual noise. The implementation leverages the ASTRA toolbox for tomographic operations. An ablation study is conducted to evaluate the sensitivity of PDM-DART to various hyperparameters across diverse phantom types. The implementation is available here[1].**

***Index Terms*—Discrete Tomography, PDM-DART, Algebraic Reconstruction Technique (ART), SIRT, Parameter Estimation, Gaussian Mixture Models (GMM), Image Reconstruction, Ablation Study.**

I. Introduction

COMPUTED Tomography (CT) is widely used for non-invasive imaging across scientific and industrial applications. While standard reconstruction methods like Filtered Back-Projection (FBP) and Simultaneous Iterative Reconstruction Technique (SIRT) perform well with ample high-quality data, they degrade under limited acquisition conditions—common in practice due to constraints like radiation dose or time.

Discrete tomography offers a powerful approach by incorporating prior knowledge that the imaged object consists of only a few distinct materials. The Discrete Algebraic Reconstruction Technique (DART) effectively combines iterative reconstruction with segmentation. However, DART traditionally assumes known grey levels and thresholds.

To overcome this limitation, Van Aarle et al. proposed the Projection Distance Minimization DART (PDM-DART)[2]. PDM-DART is an iterative algorithm that automates the estimation of optimal grey levels and segmentation thresholds by adaptively minimizing the Euclidean distance between the forward projection of the segmented intermediate reconstruction and the measured projection data. This eliminates the need for manual parameter input, aiming to make discrete tomography more robust and accessible.

Manuscript created July 1, 2025.

[1]https://github.com/GoelPri-uni/CT_Scan/tree/main

The PDM-DART algorithm provides a robust framework for adaptive parameter estimation. However, to better address real-world scenarios with unknown or variable material densities, our implementation focuses on robust initialization. We utilize phantoms with randomly initialized, varying intensities, making a priori density knowledge unavailable. Consequently, we employ Gaussian Mixture Models (GMM) [3] applied to an initial SIRT reconstruction for the initial estimation of grey levels and thresholds.

This paper details our PDM-DART implementation using the ASTRA toolbox [4], focusing on:

- Initialization of grey level ($\boldsymbol{\rho}^{(0)}$) and threshold ($\boldsymbol{\tau}^{(0)}$) parameters using GMM on an initial SIRT reconstruction ($\boldsymbol{v}^{(0)}$).
- A median filter post-processing step on the final reconstruction.
- Analysis of optimization techniques (Nelder-Mead, COBYLA, Powell) and the impact of internal SIRT iterations (t_s).

II. Phantom Description

PDM-DART adaptively estimates discrete grey levels by classifying pixels as ”fixed” (homogeneous) or ”free” (refined at boundaries/uncertain areas). While suited for objects with few materials, real-world data like medical CTs often show continuous intensity variations and gradients, challenging strictly discrete segmentation. Our phantoms are designed to test PDM-DART under these conditions. We will evaluate its response to smooth gradients versus sharp edges, its tendency for artificial quantization, and its pixel classification in complex or overlapping regions. This will help define PDM-DART's applicability beyond simple discrete objects.

We have divided our focus among four types of phantoms each designed to evaluate different aspects of segmentation and reconstruction accuracy:

- **Layered Phantom**: A star-shaped phantom designed to evaluate segmentation accuracy for sharp edges and grey-level transitions. This serves as an initial test for our method's implementation. It is constructed around a disk shape, with triangular protrusions formed by dividing angles equally using sine and cosine functions. The inner concentric ellipses (look like onion layers)have increasing intensity values starting from 0.3, with each subsequent ellipse increasing by an iterative factor of 0.1, creating a grey level gradient effect.

- **Resolution Phantom**: This phantom augments the basic star structure with small ellipses of different grey levels. It is designed to assess how the reconstruction method resolves high-frequency structures placed in close proximity.
- **CT Phantom**: An enhanced version of the Resolution phantom, the CT Phantom is designed to simulate a real CT scan of a cross-section of the human body (e.g., reproductive system), featuring various shapes representing different tissues, bones, and air pockets (see Figure 1 for visual representation, if applicable, or refer to general CT appearance). The simulated CT is built upon an elliptical base (soft tissue, intensity 0.5), with randomly placed smaller ellipses acting as organs (intensities 0.4 – 0.6). A spinal-like structure (high intensity, 0.9) and air pockets (low intensity, 0.1) are included to test the method's ability to differentiate materials. Blood vessel-like structures (intensity 0.7) are also incorporated. Shapes are placed randomly to enhance the realism of the test.
- **Filled Phantom**: This phantom is specifically designed to evaluate the method's performance on less homogeneous areas not defined by sharp boundaries. It contains random shapes like disks, ellipses, and polygons, each with different grey intensity levels (0.2 – 0.9). Curved lines (Bezier curves) are added to simulate blood vessels, testing how the method handles smooth structures and assigns pixels to fixed and free categories. The shapes are placed randomly, often overlapping, to increase the difficulty of segmentation.

III. Theoretical Background

A. Discrete Algebraic Reconstruction Technique (DART)

The Discrete Algebraic Reconstruction Technique (DART) is particularly effective when prior knowledge indicates that the object being imaged is composed of a limited number of distinct materials, each corresponding to a discrete grey level. This constraint allows DART to produce high-quality reconstructions, especially from sparse or limited-angle projection data. A typical iteration k in the DART algorithm involves:

1) Segmenting the current reconstructed image $\boldsymbol{v}^{(k)}$ into a discrete image $\boldsymbol{s}^{(k)}$ using a set of pre-defined grey levels $\boldsymbol{\rho} = \{\rho_1, \ldots, \rho_l\}^T$ and corresponding threshold values $\boldsymbol{\tau} = \{\tau_1, \ldots, \tau_{l-1}\}$.
2) Identifying "fixed" pixels (those confidently classified to a specific grey level) and "free" pixels (typically located at the boundaries between different material regions or in areas of uncertainty). Let $U^{(k)}$ be the set of indices of free pixels.
3) Constructing an image $\boldsymbol{f}^{(k)}$ where fixed pixels take values from $\boldsymbol{s}^{(k)}$ and free pixels are set to be zero.
4) Calculating a residual sinogram $\boldsymbol{r}^{(k)} = \boldsymbol{p} - \boldsymbol{W}\boldsymbol{f}^{(k)}$, compute the differnce between actual and projection sinogram, where $\boldsymbol{p}$ is the measured sinogram and $\boldsymbol{W}$ is the projection operator.
5) Updating the reconstruction by applying an iterative solver (such as SIRT [5]) to this residual sinogram, with the update confined to the free pixels $U^{(k)}$. If $S^{(t_s)}_{U^{(k)}}$ denotes t_s iterations of SIRT restricted to $U^{(k)}$, the update is $\boldsymbol{v}^{(k+1)} = \boldsymbol{f}^{(k)} + S^{(t_s)}_{U^{(k)}}\boldsymbol{r}^{(k)}$.

A significant practical challenge in applying conventional DART is the prerequisite knowledge of the exact grey levels $\boldsymbol{\rho}$ and thresholds $\boldsymbol{\tau}$.

B. Projection Distance Minimization DART (PDM-DART)

The Projection Distance Minimization DART (PDM-DART) method addresses the parameter estimation challenge by integrating an automatic and adaptive estimation step for $\boldsymbol{\rho}$ and $\boldsymbol{\tau}$ directly within each DART iteration.

1) Core Principle: Adaptive Segmentation: Instead of relying on fixed, pre-specified segmentation parameters, PDM-DART dynamically optimizes $\boldsymbol{\rho}$ and $\boldsymbol{\tau}$ at each iteration k, based on the current intermediate reconstruction $\boldsymbol{v}^{(k)}$. The optimization criterion is the minimization of the squared Euclidean distance between the forward projection of the hypothetically segmented image $C_{\boldsymbol{\tau},\boldsymbol{\rho}}(\boldsymbol{v}^{(k)})$ and the measured projection data $\boldsymbol{p}$. Mathematically, PDM-DART seeks to find the optimal segmentation parameters $\{\boldsymbol{\tau}^{(k)}_{opt}, \boldsymbol{\rho}^{(k)}_{opt}\}$ by solving:

$$\{\boldsymbol{\tau}^{(k)}_{opt}, \boldsymbol{\rho}^{(k)}_{opt}\} = \underset{\boldsymbol{\tau},\boldsymbol{\rho}}{\operatorname{argmin}} \left\| \boldsymbol{W} C_{\boldsymbol{\tau},\boldsymbol{\rho}}(\boldsymbol{v}^{(k)}) - \boldsymbol{p} \right\|_2^2 \tag{1}$$

where:

- $\boldsymbol{v}^{(k)} \in \mathbb{R}^n$ is the reconstructed image (with n pixels) at iteration k.
- $C_{\boldsymbol{\tau},\boldsymbol{\rho}}(\boldsymbol{v}^{(k)})$ segments $\boldsymbol{v}^{(k)}$ using thresholds $\boldsymbol{\tau}$ into an image with l discrete grey levels $\boldsymbol{\rho}$.
- $\boldsymbol{W}$ is the $m \times n$ projection operator matrix.
- $\boldsymbol{p} \in \mathbb{R}^m$ is the measured projection data.

This optimization is typically decomposed into two nested subproblems:

a) Inner Optimization: Grey Level Estimation: Given candidate thresholds $\bar{\boldsymbol{\tau}}$, this step finds optimal grey levels $\boldsymbol{\rho}_{opt}$. Let $s_t(\boldsymbol{v}^{(k)}, \bar{\boldsymbol{\tau}})$ be a binary mask for pixels in class t. The forward projection of the segmented image is $\boldsymbol{W} C_{\bar{\boldsymbol{\tau}},\boldsymbol{\rho}}(\boldsymbol{v}^{(k)}) = \sum_{t=1}^{l} \rho_t (\boldsymbol{W} s_t(\boldsymbol{v}^{(k)}, \bar{\boldsymbol{\tau}})) = \boldsymbol{A}(\bar{\boldsymbol{\tau}})\boldsymbol{\rho}$. The objective is:

$$\boldsymbol{\rho}_{opt}(\bar{\boldsymbol{\tau}}) = \underset{\boldsymbol{\rho}}{\operatorname{argmin}} \|\boldsymbol{A}(\bar{\boldsymbol{\tau}})\boldsymbol{\rho} - \boldsymbol{p}\|_2^2 \tag{2}$$

This is a linear least-squares problem, solved by the normal equations:

$$(\boldsymbol{A}(\bar{\boldsymbol{\tau}})^T \boldsymbol{A}(\bar{\boldsymbol{\tau}}))\boldsymbol{\rho}_{opt} = \boldsymbol{A}(\bar{\boldsymbol{\tau}})^T \boldsymbol{p} \tag{3}$$

b) Outer Optimization: Threshold Value Estimation: This step finds optimal thresholds $\boldsymbol{\tau}_{opt}$, using $\boldsymbol{\rho}_{opt}(\boldsymbol{\tau})$ from the inner optimization:

$$\boldsymbol{\tau}^{(k)}_{opt} = \underset{\boldsymbol{\tau}}{\operatorname{argmin}} \left\| \boldsymbol{W} C_{\boldsymbol{\tau},\boldsymbol{\rho}_{opt}(\boldsymbol{\tau})}(\boldsymbol{v}^{(k)}) - \boldsymbol{p} \right\|_2^2 \tag{4}$$

Since this is non-differentiable, derivative-free methods like Nelder-Mead [6], Powell [7] and COBYLA [8] are used.

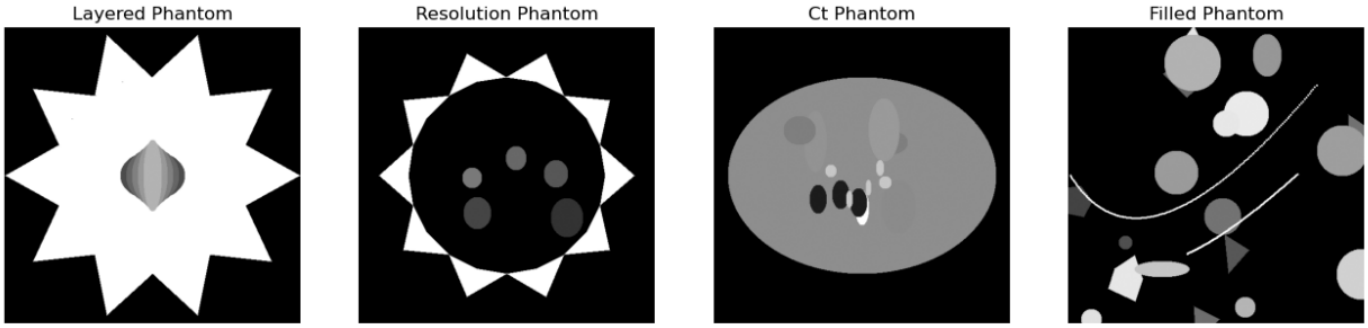

Fig. 1: Simulated phantoms for testing PDM-DART: (a) Layered, (b) Resolution, (c) CT, and (d) Filled Phantom.

c) Initial Estimation via Gaussian Mixture Model (GMM): GMM initialization was introduced to provide a good estimate at starting point for PDM-DART, improving early convergence and final segmentation accuracy. The initial reconstructed image after SIRT $\boldsymbol{v}^{(0)}$ is flattened, and extreme intensity values (e.g., outside the 1st and 99th percentiles) may be removed to improve GMM fitting. A GMM with l components (where l is the expected number of distinct materials/grey levels) is fitted to the pixel intensity distribution. The means of the fitted Gaussians, once sorted, become the initial grey levels $\boldsymbol{\rho}^{(0)} = (\rho_1^{(0)}, \ldots, \rho_l^{(0)})^T$. The initial thresholds $\boldsymbol{\tau}^{(0)} = (\tau_1^{(0)}, \ldots, \tau_{l-1}^{(0)})$ are then set as the midpoints between adjacent sorted grey levels:

$$\tau_j^{(0)} = \frac{\rho_j^{(0)} + \rho_{j+1}^{(0)}}{2}, \quad \text{for } j = 1, \ldots, l-1 \tag{5}$$

This probabilistic initialization provides a more robust and data-driven starting point.

IV. Methodology

Our implementation of the PDM-DART algorithm follows the iterative scheme outlined in Section III, incorporating specific choices for initialization, optimization, and post-processing, aimed at enhancing robustness and final image quality.

A. Algorithmic Framework

The implemented PDM-DART algorithm iteratively refines an image estimate $\boldsymbol{v}^{(k)}$ (a vector of pixel values) at DART iteration k. The overall process is as follows:

1. **Initialization Phase:**

(a) *Initial SIRT Reconstruction:* An initial image estimate $\boldsymbol{v}^{(0)}$ is obtained by applying a t_s number of SIRT iterations to the measured sinogram$\boldsymbol{p}$.

(b) *GMM-based Parameter Estimation:* The initial grey levels $\boldsymbol{\rho}^{(0)}$ and thresholds $\boldsymbol{\tau}^{(0)}$ are estimated $\boldsymbol{v}^{(0)}$ using Gaussian Mixture Models (GMM) as described in Section III.

2. **Iterative PDM-DART Loop:** For each DART iteration$k = 0, \ldots, N_{DART} - 1$:

(a) *Adaptive Parameter Optimization (PDM Step):* The grey levels $\boldsymbol{\rho}^{(k)}$ and thresholds $\boldsymbol{\tau}^{(k)}$ are not updated at every iteration, as frequent updates may introduce noise. Instead, they are optimized every uf iteration, i.e., whenever $k \bmod uf = 0$ or $k = 0$. This involves solving the nested optimization problem described by Eq. (1):

- **Inner Optimization:** For a given $\bar{\boldsymbol{\tau}}$, optimal grey levels $\boldsymbol{\rho}_{opt}(\bar{\boldsymbol{\tau}})$ are found by solving Eq. (2) via Eq. (3).
- **Outer Optimization:** Optimal thresholds $\boldsymbol{\tau}_{opt}^{(k)}$ are found by solving Eq. (4) using a chosen derivative-free optimizer (e.g., Nelder-Mead, COBYLA, or Powell). The corresponding grey levels are $\boldsymbol{\rho}_{opt}^{(k)} = \boldsymbol{\rho}_{opt}(\boldsymbol{\tau}_{opt}^{(k)})$.

(b) *Image Segmentation:* The current continuous reconstruction $\boldsymbol{v}^{(k)}$ is segmented into a discrete image $\boldsymbol{s}^{(k)}$ using the currently active (optimized or carried-over) grey levels $\boldsymbol{\rho}^{(k)}$ and thresholds $\boldsymbol{\tau}^{(k)}$:

$$\boldsymbol{s}^{(k)} = C_{\boldsymbol{\tau}^{(k)}, \boldsymbol{\rho}^{(k)}}(\boldsymbol{v}^{(k)}) \tag{6}$$

This operation assigns each pixel in $\boldsymbol{v}^{(k)}$ to the grey level $\rho_j^{(k)}$ whose corresponding interval $[\tau_{j-1}^{(k)}, \tau_j^{(k)})$ (with $\tau_0^{(k)} = -\infty, \tau_l^{(k)} = +\infty$) contains the pixel's value.

(c) *Update Mask Generation:* A binary mask $\boldsymbol{M}_{update}^{(k)}$ is created to identify pixels eligible for updates. Let $N(j)$ be the set of 4-connected neighbors of pixel j.

- **Boundary Pixels:** Pixel j is a boundary pixel if $s_j^{(k)} \neq s_h^{(k)}$ for at least one neighbor $h \in N(j)$. All boundary pixels are included in $\boldsymbol{M}_{update}^{(k)}$.
- **Random Pixels:** A small percentage (e.g., 5%) of non-boundary pixels are randomly selected and also included in $\boldsymbol{M}_{update}^{(k)}$.

(d) *Residual Sinogram Calculation:* An intermediate image $\boldsymbol{f}^{(k)}$ is formed:

$$f_j^{(k)} = \begin{cases} s_j^{(k)} & \text{if pixel } j \notin \boldsymbol{M}_{update}^{(k)} \\ 0 & \text{if pixel } j \in \boldsymbol{M}_{update}^{(k)} \end{cases} \tag{7}$$

The residual sinogram $\boldsymbol{r}^{(k)}$ is then computed as:

$$\boldsymbol{r}^{(k)} = \boldsymbol{p} - \boldsymbol{W}\boldsymbol{f}^{(k)} \tag{8}$$

(e) *SIRT Update on Residual:* The residual sinogram $\boldsymbol{r}^{(k)}$ is reconstructed using t_s iterations of SIRT, with updates restricted to pixels in $\boldsymbol{M}_{update}^{(k)}$. Let this update be $\Delta\boldsymbol{v}^{(k)} = S_{\boldsymbol{M}_{update}^{(k)}}^{(t_s)}(\boldsymbol{r}^{(k)})$.

(f) *Image Update:* The reconstruction is updated:

$$\boldsymbol{v}^{(k+1)} = \boldsymbol{f}^{(k)} + \Delta\boldsymbol{v}^{(k)} \tag{9}$$

(g) *Regularization:* A Gaussian smoothing filter is applied to $\boldsymbol{v}^{(k+1)}$ to regularize the solution and improve stability before the next DART iteration.

3. **Post-processing:** After N_{DART} iterations, a final median filter (e.g., with a 5x5 kernel) is applied to the resulting reconstruction $\boldsymbol{v}^{(N_{DART})}$. This extension was added as DART-based methods, while good at preserving edges, can sometimes leave behind or introduce small, isolated noise-like artifacts (salt-and-pepper noise). The median filter is effective at removing such noise while generally preserving significant structural edges, aiming for a visually cleaner final image without substantially degrading the core reconstruction quality.

B. Evaluation Metrics

To evaluate the quality of image reconstruction, we employed the following metrics:

a) Root Mean Square Error (RMSE):: The RMSE measures the average magnitude of pixel-wise differences between the reconstructed image $\hat{x}$ and the ground truth phantom x:

$$\text{RMSE} = \sqrt{\frac{1}{N}\sum_{i=1}^{N}(x_i - \hat{x}_i)^2} \tag{10}$$

Where N is the total number of pixels, x_i is the true pixel value, and $\hat{x}_i$ is the reconstructed pixel value. This metric is particularly useful for comparing reconstructions across different phantom types or intensity scales, as it provides a normalized view of error, with a bigger penalty on outlier scenarios.

V. Experiments

The goal of this experiment is to evaluate the sensitivity of the PDM-DART reconstruction algorithm to each hyperparameter and to understand their impact on reconstruction quality over simulated phantoms. To achieve this, we iteratively performed the ablation study on each phantom in Figure 1 by varying one hyperparameter at a time while keeping the others fixed. After identifying the best value for a given parameter (based on reconstruction performance using RMSE), we updated the default setting and proceeded to the next parameter. We also conducted an additional experiment on using the PDM-DART with GMM and Post processing in comparison to using PDM-DART knowing only the minimum and maximum grey level present.

A. Hyperparameter Settings

The initial default settings used in the experiments are Number of grey levels (l):10, PDM iterations (N_{DART}): 30, SIRT iterations (t_s): 40, Update frequency (uf): 5, Detector size factor: 4. The following hyperparameters were varied during the ablation study:

TABLE I: Hyperparameters and Their Tested Values

Parameter	**Values**
Optimization method	{Nelder-Mead, Powell, COBYLA}
Number of grey levels (l)	{5, 10, 15}
Number of PDM iterations (N_{DART})	{10, 30, 60, 80}
Number of SIRT iterations (t_s)	{20, 40, 50}
Update frequency (uf)	{5, 10, 15}
Detector size factor	{2, 4, 6}

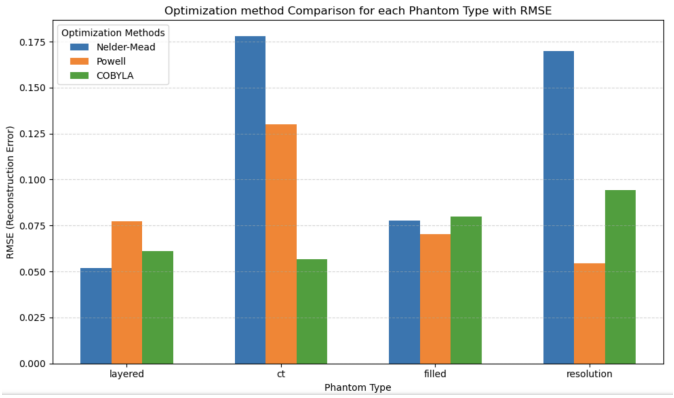

Fig. 2: RMSE for different optimization methods across phantom types.

B. Results

1) Effect of Optimization Method on Reconstruction Quality: To investigate the effect of the optimizer used for threshold tuning in PDM-DART, we performed an ablation study comparing three optimization strategies: **Nelder-Mead**, **Powell**, and **COBYLA**. Figure 2 shows the RMSE values across different optimization methods for each phantom type. We observe that the choice of optimizer has a significant impact on reconstruction accuracy, especially for more complex phantoms; hence, we perform this as our first ablation.

- For the **Layered**, we see Nelder-Mead (RMSE=0.052) performed the best compared to COBYLA and Powell. Our possible understanding is that Nelder-Mead is highly sensitive to shift in change, and hence it might have been more useful in case of optimizing the grey levels, especially for onion rings. In the case of **CT** phantom, compared to Nelder-Mead and Powell, **COBYLA** performed slightly better (RMSE $= 0.056$).
- The **Filled** phantom had a better performance with **Powell** optimizer, reducing RMSE from 0.077 (Nelder-Mead) to 0.070.
- In the **Resolution** phantom, the **Powell** optimizer significantly outperformed the others, achieving the lowest RMSE of 0.054, compared to 0.169 (Nelder-Mead) and 0.09 (COBYLA).

2) Number of Grey Levels (l): The number of grey levels used in the PDM-DART algorithm determines the discretization granularity during segmentation and reconstruction. The results, shown in Fig. 3, demonstrate the following insights:

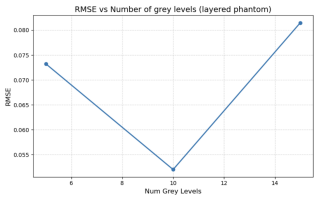

(a) Layered phantom

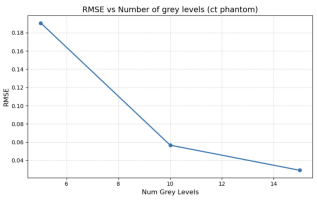

(b) Ct phantom

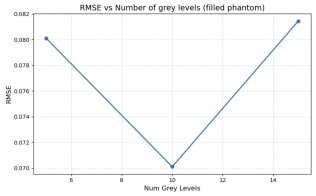

(c) Filled phantom

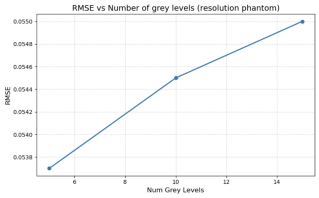

(d) Resolution phantom

Fig. 3: RMSE comparisons under grey level settings of 5,10,15.

- **Layered and Filled phantoms:** Both performed best with 10 grey levels. For the Layered 3aphantom, RMSE decreased from 0.073 (5 levels) to 0.052 (10 levels), then increased to 0.082 (15 levels). A similar trend was observed for the Filled 3c phantom, achieving the lowest RMSE of 0.07 at 10 grey levels. This suggests an optimal trade-off at intermediate discretization.
- **CT phantom:** Reconstruction quality improved as the number of grey levels increased from 5 (RMSE = 0.191) to 15 (0.0292), achieving the lowest at 15 grey levels for CT 3b
- **Resolution phantom Figure 3d:** The RMSE was lowest with 5 grey levels (0.0537), and increasing to 10 or 15 levels degraded the performance, indicating 5 to be the optimal number of grey levels required for experiments.

3) Number of PDM Iterations(N_{DART}):

- In Figure 5, the **Layered** (Fig. 5a) phantom initially shows a stable RMSE, which then gradually decreases to reach a minimum around 80 iterations (RMSE=0.052). Based on this trend, 80 PDM iterations was chosen for further experiments.
- In contrast, the **CT** (Fig. 5b) phantom exhibits an RMSE that initially rises, peaking near 60 iterations, after which it begins to decline. In the case of CT result, although we saw minimum RMSE at 10 PDM iterations, we used PDM with 80 iterations. As seen in Figure 4, PDM of 80 iterations captured more elements inside the outer ellipse with higher concentration, although it is 0.002 units noisier compared to PDM of 10 iterations.
- The **Filled** (Fig. 5c), phantom demonstrates a more consistent trend, with the RMSE generally decreasing as the number of PDM iterations increases, suggesting ongoing refinement within the observed range. Hence, we use 80 PDM iterations for later use.
- Finally, the **Resolution** (Fig. 5d) phantom displays a U-shaped RMSE curve, achieving its lowest error around 30 iterations and then increasing with further iterations. Hence, we use 30 PDM iterations for further experiments.

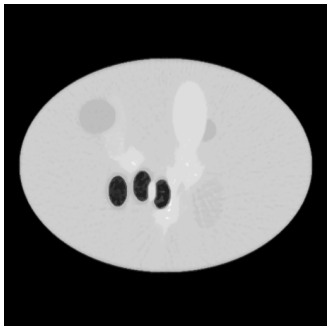

(a) 10 PDM iterations.

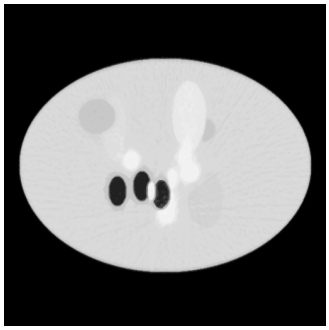

(b) 80 PDM iterations.

Fig. 4: CT phantom reconstruction: qualitative comparison for N_{DART}.

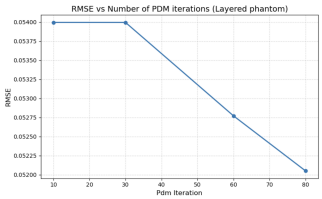

(a) Layered phantom

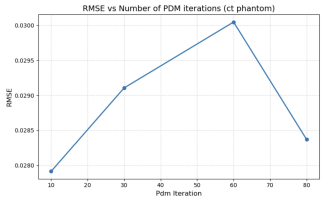

(b) Ct phantom

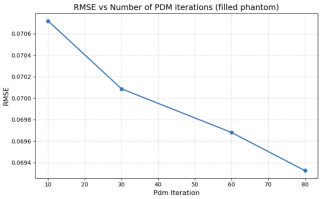

(c) Filled phantom

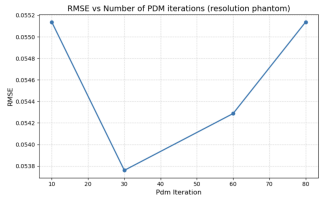

(d) Resolution phantom

Fig. 5: RMSE comparisons under pdm iterations (N_{DART}).

4) Number of SIRT Iterations (t_s): For the Layered and Filled phantoms in Figure 7, increasing internal SIRT iterations from 20 to 40 substantially reduced the RMSE. However, a further increase to 50 iterations resulted in a slight increase in RMSE, suggesting an optimal around 40 iterations for these cases. As seen in Figure 6, we can observe a significant impact of the number of SIRT iterations in the reconstruction process on the layered phantom. With SIRT of 50 iterations, although we had good onion rings, we can observe noisy projection lines observed in the outer areas. In the case of SIRT with 20 iterations, the onion rings are still in the process of construction, and we can see a more robust structure with SIRT of 40 iterations. In contrast, for the CT and Resolution in Figure 7 phantoms, a consistent trend of decreasing RMSE was observed as internal SIRT iterations increased from 20 to 50, with the lowest RMSE achieved at 50 iterations within the tested range. This indicates that these more complex phantoms may benefit from a higher number of internal SIRT updates.

5) Value of Update Frequency (uf): For the phantoms of layered 8a, filled 8c and resolution 8d, performing the PDM update every 10 iterations (uf = 10) resulted in the highest RMSE, indicating a less optimal reconstruction. More frequent updates (every 5 iterations) or less frequent updates (every 15 iterations) yielded lower, and often comparable, RMSE values

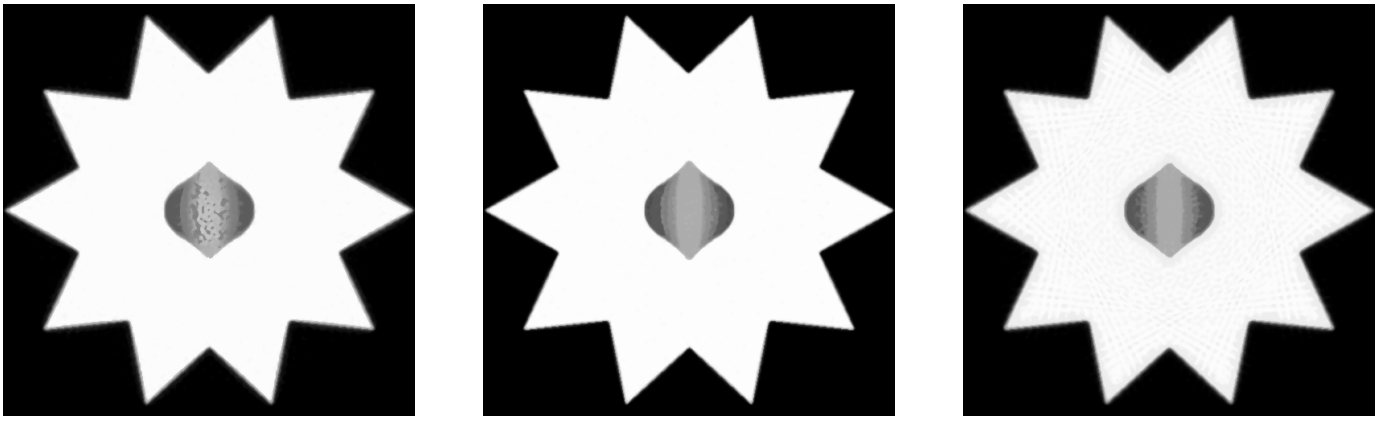

(a) $t_s = 20$ (b) $t_s = 40$ (c) $t_s = 50$

Fig. 6: Effect of SIRT iterations (t_s) on reconstruction in Layered phantom.

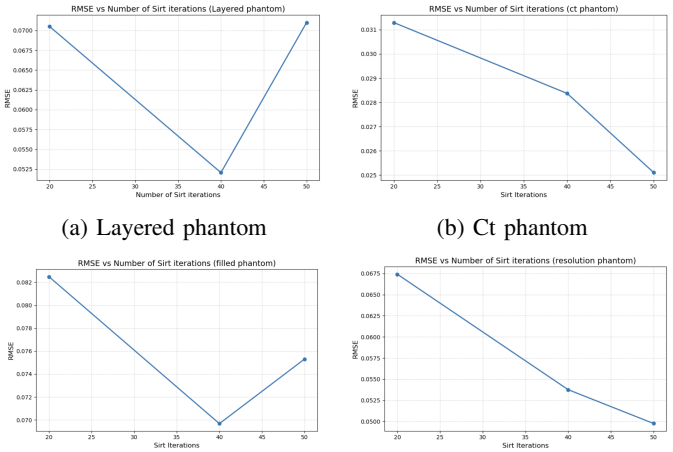

(a) Layered phantom (b) Ct phantom

(c) Filled phantom (d) Resolution phantom

Fig. 7: RMSE comparisons under sirt iterations (t_s).

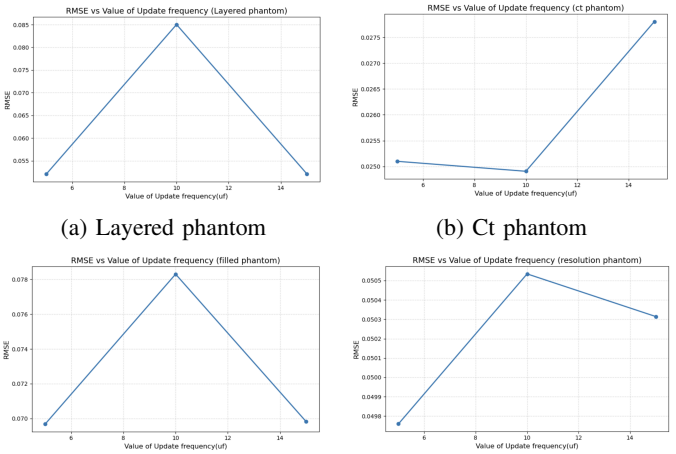

(a) Layered phantom (b) Ct phantom

(c) Filled phantom (d) Resolution phantom

Fig. 8: RMSE comparisons under varying Update frequency (uf).

for these phantoms. This suggests that an intermediate update frequency might be detrimental, possibly due to parameters not settling optimally before the next adjustment.

The CT phantom 8b showed a slightly different trend, with the lowest RMSE achieved when updating every 10 iterations. More frequent updates (every 5 iterations) were slightly worse, and less frequent updates (every 15 iterations) led to a significant increase in RMSE.

6) Number of varying detector sizes: For the Layered 9a, Filled 9c, and Resolution 9d phantoms, a Detector Size Factor of 4 consistently yielded the lowest RMSE. Using a smaller factor (2) or a larger factor (6) resulted in higher RMSE values, indicating that a factor of 4 provides an optimal balance for sampling these particular phantom structures. The CT phantom 9b also showed improvement when increasing the factor from 2 to 4. Interestingly, a further increase to a factor of 6 resulted in a slight additional reduction in RMSE, suggesting that for this more complex phantom, finer sampling (larger detector size factor) continues to be beneficial within the tested range.

7) Impact on Phantom reconstruction accuracy with GMM and Post-Processing (PP): As seen in figure 10 compares

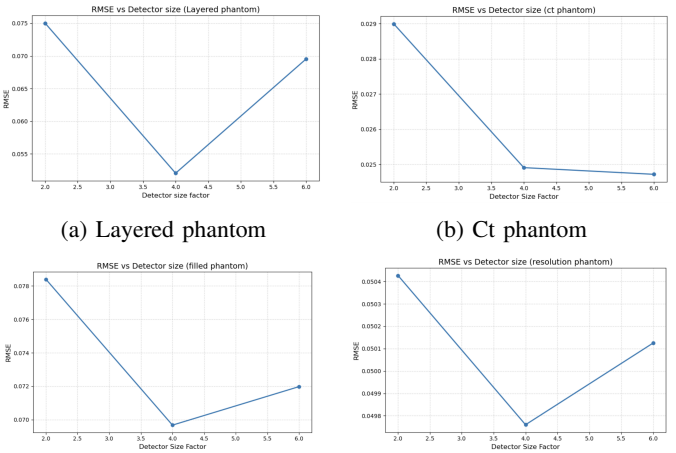

(a) Layered phantom (b) Ct phantom

(c) Filled phantom (d) Resolution phantom

Fig. 9: RMSE comparisons under varying detector sizes.

RMSE values for PDM-DART with and without the proposed GMM initialization and median filter post-processing (PP).

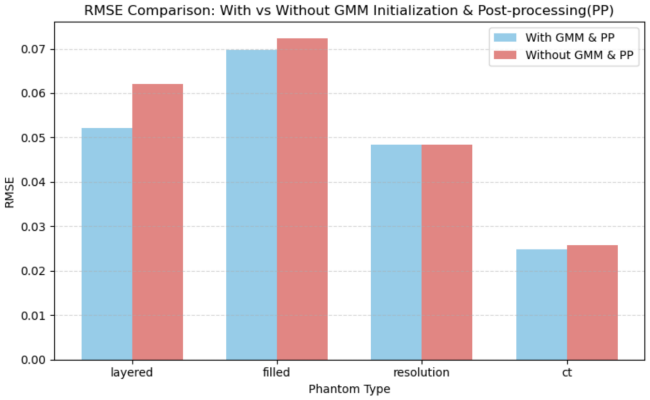

Fig. 10: Comparison of PDM-DART with GMM & PP vs. without.

Across all four phantoms—Layered, Filled, Resolution, and CT—the enhanced version (blue bars) consistently achieved lower RMSE than the baseline (red bars). The improvement was most notable for the Layered and Filled phantoms, while CT and Resolution showed smaller but consistent gains. These results highlight the effectiveness of GMM for data-driven initialization and median filtering for refinement, improving reconstruction accuracy across varying phantom complexities.

C. Discussion

Our ablation study highlights that PDM-DART performance is highly sensitive to phantom complexity, with no universally optimal hyperparameter configuration. The optimization method used for threshold estimation showed clear phantom-specific preferences: Nelder-Mead performed best for the smooth, concentric-layered structure of the Layered phantom; COBYLA was optimal for the highly detailed and textured CT phantom; and Powell performed best for the Filled and Resolution phantoms, which contain sharp boundaries and high-frequency features. The number of grey levels (l) exhibited a complexity-dependent trade-off: simpler phantoms (Layered, Filled) favored intermediate levels ($l = 10$), while the CT phantom improved with more levels ($l = 15$), and the Resolution phantom performed best with fewer ($l = 5$), likely to avoid over-parameterization. PDM iterations (N_{DART}) demonstrated that while the Filled phantom continued to improve up to 80 iterations, other phantoms exhibited optimal stopping points beyond which RMSE increased, suggesting risks of overfitting or divergence. Especially in the case of CT reconstruction, the indication of actuall performance differed from the RMSE value, possibly due to the more details that were reconstructed, and then the prediction outlier increased, which is the limitation of RMSE. Similarly, internal SIRT iterations (t_s) showed that complex phantoms like CT benefited from more updates (up to 50), while simpler ones peaked earlier. The update frequency (uf) influenced stability, with most phantoms disfavoring intermediate updates (every 10 iterations), except for the CT phantom, which uniquely improved under this setting. Finally, the detector size factor affected the resolution of projection data, with a value of 4 being broadly optimal, while the CT phantom again benefited from finer sampling (factor 6). These results emphasize the importance of aligning PDM-DART hyperparameters with the structural and material complexity of the object being reconstructed. Qualitative evaluation revealed certain limitations. For the CT phantom reconstruction, achieving the expected grey level distribution and sharp boundaries for fine structures proved challenging, suggesting difficulties in precisely segmenting subtle or closely packed features. Similarly, while the Layered phantom's 'onion ring' reconstruction has the correct number of layers, the boundaries between these gradient steps were blurred, indicating that discretizing smooth transitions into sharply defined levels remains an area for improvement.

VI. Future Work

Future work will focus on enhancing PDM-DART by exploring more sophisticated global optimization strategies (such as Bayesian or evolutionary algorithms) for the PDM step, potentially alongside investigating gradient-based methods if suitable differentiable approximations can be found. Additionally, improving the algorithm's capacity to handle continuous intensity variations is crucial; this could involve developing hybrid discrete-continuous models or adaptive techniques for local grey level (l) estimation. Finally, integrating advanced regularization methods, like discrete-aware Total Variation, or more sophisticated edge-preserving filters within the DART framework could lead to sharper boundary definition and reduced artifacts, particularly for complex structures and smooth gradients.

VII. Conclusion

This work successfully implemented the PDM-DART algorithm, enhanced with GMM-based initialization and median filtering, using the ASTRA toolbox for high-quality tomographic reconstruction. Through a comprehensive ablation study across diverse phantoms, we demonstrated that while PDM-DART effectively automates grey level and threshold estimation, its performance can be significantly enhanced through careful tuning of key hyperparameters. Importantly, the study revealed that optimal configurations are phantom-dependent, reflecting the adaptability of PDM-DART to a wide range of imaging challenges. Despite minor limitations in resolving fine or smooth structures, particularly in complex phantoms, the framework consistently produced high-fidelity reconstructions. These insights open promising directions for future improvements, including integrating global optimization techniques, hybrid intensity models, and advanced regularization, to further strengthen PDM-DART as a versatile and robust tool for discrete tomography.

References

[1] K. J. Batenburg and J. Sijbers, "Dart: A practical reconstruction algorithm for discrete tomography," *IEEE Transactions on Image Processing*, vol. 20, no. 9, pp. 2542–2553, 2011.

[2] W. van Aarle, K. J. Batenburg, and J. Sijbers, "Automatic parameter estimation for the discrete algebraic reconstruction technique (dart)," *IEEE Transactions on Image Processing*, vol. 21, no. 11, pp. 4608–4621, 2012.

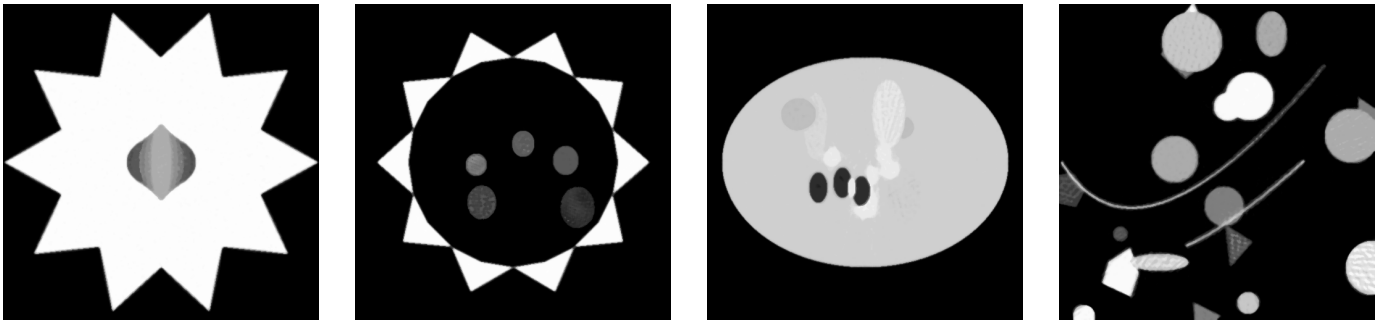

(a) Layered Phantom (b) Resolution phantom (c) Ct phantom (d) Filled phantom

Fig. 11: Final reconstructed phantoms using PDM-DART with GMM.

[3] L. Zhao, S. Zheng, W. Yang *et al.*, "An image thresholding approach based on gaussian mixture model," *Pattern Analysis and Applications*, vol. 22, pp. 75–88, 2019.
[4] W. van Aarle, W. J. Palenstijn, J. Cant, E. Janssens, F. Bleichrodt, A. Dabravolski, J. D. Beenhouwer, K. J. Batenburg, and J. Sijbers, "Fast and flexible x-ray tomography using the astra toolbox," *Opt. Express*, vol. 24, no. 22, pp. 25 129–25 147, Oct 2016. [Online]. Available: https://opg.optica.org/oe/abstract.cfm?URI=oe-24-22-25129
[5] J. Gregor and T. Benson, "Computational analysis and improvement of sirt," *IEEE Transactions on Medical Imaging*, vol. 27, no. 7, pp. 918–924, 2008.
[6] J. C. Lagarias, J. A. Reeds, M. H. Wright, and P. E. Wright, "Convergence properties of the nelder–mead simplex method in low dimensions," *SIAM Journal on Optimization*, vol. 9, no. 1, pp. 112–147, 1998.
[7] M. J. D. Powell, "An efficient method for finding the minimum of a function of several variables without calculating derivatives," *The Computer Journal*, vol. 7, no. 2, pp. 155–162, 1964.
[8] ——, "A direct search optimization method that models the objective and constraint functions by linear interpolation," in *Advances in Optimization and Numerical Analysis*, S. Gomez and J.-P. Hennart, Eds. Dordrecht: Kluwer Academic Publishers, 1994, pp. 51–67.